

# Quasi One-Dimensional Metal–Semiconductor Heterostructures

S. Benter,<sup>†,‡</sup> V. G. Dubrovskii,<sup>§</sup> M. Bartmann,<sup>†</sup> A. Campo,<sup>||</sup> I. Zardo,<sup>||</sup> M. Sistani,<sup>†</sup> M. Stöger-Pollach,<sup>⊥</sup> S. Lancaster,<sup>†</sup> H. Detz,<sup>†,#</sup> and A. Lugstein<sup>\*,†,||</sup>

<sup>†</sup>Institute of Solid State Electronics, TU Wien, Gußhausstraße 25-25a, 1040 Vienna, Austria

<sup>‡</sup>Division of Synchrotron Radiation Research, Lund University, Sölvegatan 14, 221 00 Lund, Sweden

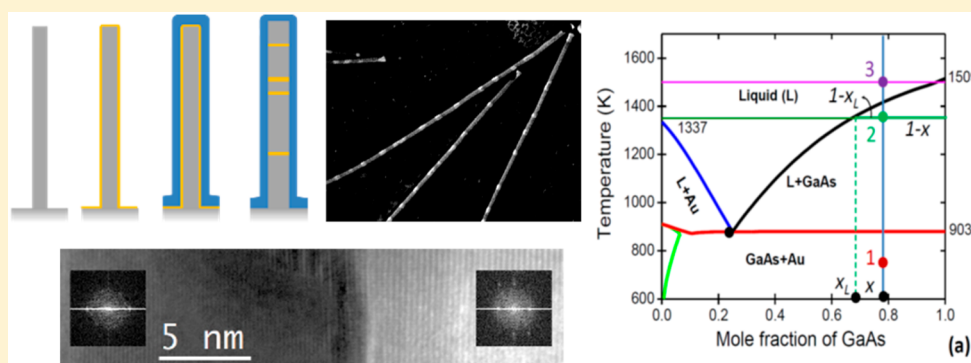
<sup>§</sup>ITMO University, Kronverkskiy pr. 49, 197101 St. Petersburg, Russia

<sup>||</sup>Department of Physics, University of Basel, Klingelbergstrasse 82, 4056 Basel, Switzerland

<sup>⊥</sup>University Service Center for TEM, TU Wien, Wiedner Hauptstraße 8-10, 1040 Vienna Austria

<sup>#</sup>Central European Institute of Technology, Brno University of Technology, Purkyňova 123, 612 00 Brno, Czech Republic

**S** Supporting Information



**ABSTRACT:** The band offsets occurring at the abrupt heterointerfaces of suitable material combinations offer a powerful design tool for high performance or even new kinds of devices. Because of a large variety of applications for metal–semiconductor heterostructures and the promise of low-dimensional systems to present exceptional device characteristics, nanowire heterostructures gained particular interest over the past decade. However, compared to those achieved by mature two-dimensional processing techniques, quasi one-dimensional (1D) heterostructures often suffer from low interface and crystalline quality. For the GaAs–Au system, we demonstrate exemplarily a new approach to generate epitaxial and single crystalline metal–semiconductor nanowire heterostructures with atomically sharp interfaces using standard semiconductor processing techniques. Spatially resolved Raman measurements exclude any significant strain at the lattice mismatched metal–semiconductor heterojunction. On the basis of experimental results and simulation work, a novel self-assembled mechanism is demonstrated which yields one-step reconfiguration of a semiconductor–metal core–shell nanowire to a quasi 1D axially stacked heterostructure via flash lamp annealing. Transmission electron microscopy imaging and electrical characterization confirm the high interface quality resulting in the lowest Schottky barrier for the GaAs–Au system reported to date. Without limiting the generality, this novel approach will open up new opportunities in the syntheses of other metal–semiconductor nanowire heterostructures and thus facilitate the research of high-quality interfaces in metal–semiconductor nanocontacts.

**KEYWORDS:** Nanowire, GaAs, gold, metal–semiconductor heterostructure, quasi 1D contacts

Since the first proposal of Schottky and Mott on metal–semiconductor interfaces<sup>1–4</sup> as well as band gap engineering by stacking layers of different semiconductors, which is the insight that won Kroemer and Alferov the Nobel Prize in Physics in 2000, heterostructures have become a cornerstone in applied and fundamental semiconductor research. The great success of semiconductor superlattices is exemplified by high electron mobility transistors<sup>5</sup> or quantum cascade lasers<sup>6</sup> based on multiquantum well structures. Improved growth of quantum dots and wires based on immense developments in synthesis and processing techniques brought further new

aspects to heterostructure and quantum well physics. These low-dimensional nanostructures enable exploitation of quantum confinement effects for engineering electronic states with custom-designed properties. However, manufacturing of axial heterostructures in quasi 1D nanowires (NWs) still faces technological challenges that prevent full realization of these advantages. Conventional methods like molecular beam

**Received:** March 15, 2019

**Revised:** May 16, 2019

**Published:** May 22, 2019

epitaxy (MBE),<sup>7–10</sup> vapor–liquid–solid,<sup>11,12</sup> metal–organic chemical vapor deposition (CVD),<sup>13,14</sup> and related methods suffer from limitations with respect to lattice matching, epitaxial integration, interface grading, and in retaining the NW morphology.<sup>15</sup> Just recently IBM demonstrated the controlled growth of NW heterostructures with abrupt interfaces for III–V semiconductors on silicon, achieved via template-assisted selective area epitaxy.<sup>16–18</sup> However, the fabrication of quasi 1D heterostructures, consisting of crystalline semiconductor material and metal, posed a major obstacle in the past. Refinement of quasi 1D superlattices or periodic structures of semiconducting and metallic layers would push forward hybrid devices for, for example, spintronics, plasmonics, and high-performance metal base transistors.

Consequently, in this work we present a general approach for the formation of quasi 1D axial metal–semiconductor NW heterostructures with epitaxial relationship and sharp interfaces. We discuss in detail the formation process for an important material system of GaAs–Au. Furthermore, the feasibility of the method for other material combinations such as Si–Au, Si–NiSi, and Si–Sn is demonstrated in the Supporting Information (Figure S1).

Figure 1 schematically displays the key manufacturing steps applied for the formation of GaAs–Au NW heterostructures

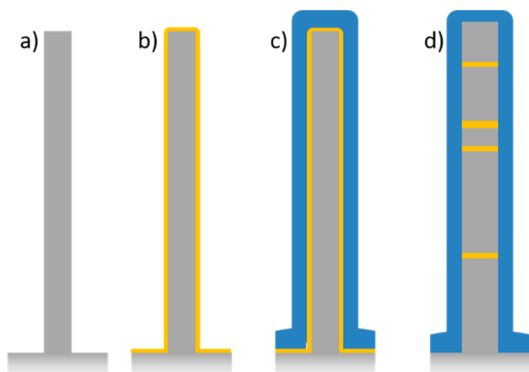


**Figure 1.** Schematics of NW heterostructure formation: (a)  $\langle 111 \rangle$ -oriented GaAs NW without native oxide, epitaxially grown on a Si substrate. (b) Deposition of a 2 nm thick Au layer via plasma enhanced sputtering. (c) Formation of 20 nm thick  $\text{SiO}_2$  shell via PE-CVD. (d) The resulting axial metal–semiconductor NW heterostructure after FLA.

employing standard semiconductor processing techniques and flash lamp annealing (FLA). Using these mature techniques, we are able to process wafer-scale samples and at the same time maintain the excellent control over the NW morphology. The starting point is an array of  $\langle 111 \rangle$ -oriented GaAs NWs, epitaxially grown on a Si substrate via MBE using the self-catalyzed vapor–liquid–solid method<sup>19</sup> (Figure 1a). The as grown NWs are about 6  $\mu\text{m}$  long, 65 nm in diameter and moderately Si-doped ( $\sim 1 \times 10^{18} \text{ cm}^{-3}$ ). After removing the native oxide, the metallic constituent is introduced by sputter deposition of a nominally 2 nm thick Au layer onto the NWs, resulting in the GaAs–Au core–shell NWs shown in Figure 1b. Subsequently, the radial GaAs–Au NWs are enclosed in a 20 nm thick silicon oxide shell using plasma-enhanced CVD (Figure 1c). The final axially stacked semiconductor–metal NW heterostructure (Figure 1d) is formed by melting and instantaneous reconfiguration of the NW core during a 20 ms

flash with an energy impact of 40  $\text{J}/\text{cm}^2$ . The FLA energy as well as the preheating of the sample before FLA were carefully adjusted to ensure complete melting of the encapsulated GaAs–Au NW core (full details of the process are given in Methods and the Supporting Information).

This processing technique is similar to the rapid melt growth,<sup>20–23</sup> first used by Liu et al.<sup>20</sup> for obtaining high-quality Ge-on-insulator structures on Si substrates and then extended to other material systems including ternary InGaAs.<sup>22</sup> The rapid melt growth method also uses  $\text{SiO}_2$  microcrucibles to contain the liquid Ge or InGaAs during the crystallization anneal. The novelty of our approach is in (i) adding the noble metal (Au) to GaAs semiconductor and (ii) designing an optimized procedure for making axial semiconductor–metal heterostructures in quasi 1D NW geometry.

The SEM image in Figure 2a shows an individual GaAs–Au NW heterostructure and the sketch above emphasizes the

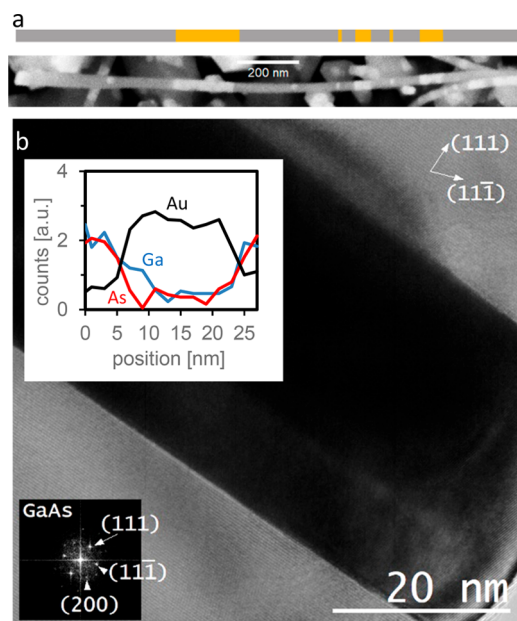


**Figure 2.** (a) SEM image of a GaAs NW with brighter gold segments of different lengths (FLA process: preheating for 10 min at 573 K, flash energy of 40  $\text{J}/\text{cm}^2$ ). The sketch above emphasizes the position of the Au segments. (b) HR-TEM analysis of the GaAs–Au interface, where Au is displayed as a darker phase. Insets: EDX-line scan across the segment (top), FFT pattern of the GaAs section close to the interface (bottom).

position of the Au segments, because the oxide shell enables only a modest SEM image quality. Several Au segments of different lengths are incorporated along the morphologically intact GaAs NW with apparently abrupt interfaces.

For structural and compositional analysis of the axial GaAs–Au NW heterostructures, TEM investigations were carried out on the Au segment shown in Figure 2b. An EDX line scan over the segment was performed to determine the two diverse phases. Evaluation of EDX counts for Ga, As, and Au are displayed in the top inset and clearly identifies GaAs as the NW material and Au in the segment. The GaAs–Au interface, for which the compositional profile is shown in the main panel of Figure 2b, appears almost atomically sharp and the determined lattice spacings of the  $\langle 111 \rangle$  planes of GaAs (0.33 nm) and Au (0.23 nm) are in good agreement with tabulated values.<sup>24,25</sup> The lattice planes of both GaAs segments

adjacent to the Au segment appeared to run parallel and the crystalline Au segments form heteroepitaxially on the  $\langle 111 \rangle$  GaAs lattice planes. This was determined via high-resolution TEM analysis and is discussed further in the [Supporting Information](#).

With respect to the formation mechanism, the complete rearrangement of the initial metal–semiconductor core–shell to an axially stacked heterostructure leads us to assume a complete meltdown of the GaAs–Au NW during FLA. Subsequent recrystallization facilitates the self-assembly of the axial metal–semiconductor heterostructure to minimize the surface area of the GaAs–Au interface. Therefore, it is essential to provide a solid shell with a higher melting point, which serves as a stable template for recrystallizing the core NW. With a melting point of approximately 1980 K,<sup>26</sup> SiO<sub>2</sub> represents an excellent shell material for GaAs and Au, whose melting temperatures are lower. Experiments performed with the same FLA power and preheating but without the SiO<sub>2</sub> shell led to the loss of the 1D NW shape due to complete melting. Furthermore, the high transparency of SiO<sub>2</sub> guarantees that most of the light is absorbed in the NW core, enabling effective heating.

The melting of the core can also be observed along the fully featured axial GaAs–Au NW heterostructures with the SiO<sub>2</sub> shell for successive FLA cycles. In particular, [Figure 3](#) displays

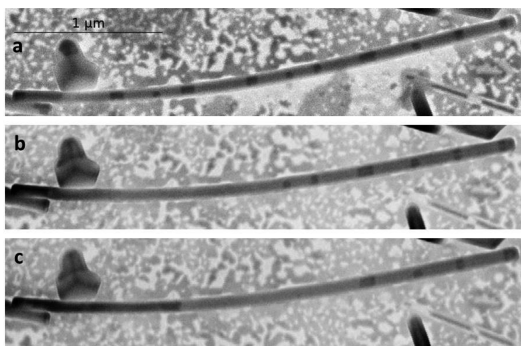


**Figure 3.** Experiment with multiple flashes on the same NW with a FLA energy of 40 J/cm<sup>2</sup> in each flash. SEM images after (a) 1st flash, (b) 5th flash, and (c) 7th flash. Because of inverse coloring, Au appears as the darker phase. Segments in the middle of the NW dissolve progressively and a larger Au segment forms at the left end of the NW. The moderate quality of the SEM images and diffuse Au–GaAs interfaces are due to the stabilizing SiO<sub>2</sub> shell, which induces charging of the samples during imaging.

exemplarily a distinct NW after the first, fifth and seventh flash. It is evident that Au segments rearrange under repeated flashes by dissolving from the middle of the NW and forming a larger segment at the left end. By considering the diffusion coefficients of Au in liquid and solid GaAs of  $<10^{-7}$  cm<sup>2</sup>/s and  $>10^{-20}$  cm<sup>2</sup>/s, respectively,<sup>27</sup> rearrangement of the segments requires a core in the liquid state to facilitate Au diffusion over a micron length within less than 20 ms of FLA (see [Figure 5b](#)).

For FLA without preheating of the substrate, the overall energy entry is lower. A heat flow from the NWs to the substrate, which acts as a heat sink, may establish a temperature gradient along the NWs. The SEM image in [Figure 4a](#) shows that the total number of Au segments is larger in the absence of preheating. Furthermore, several superficial Au clusters remain at the NW surface rather than intercept

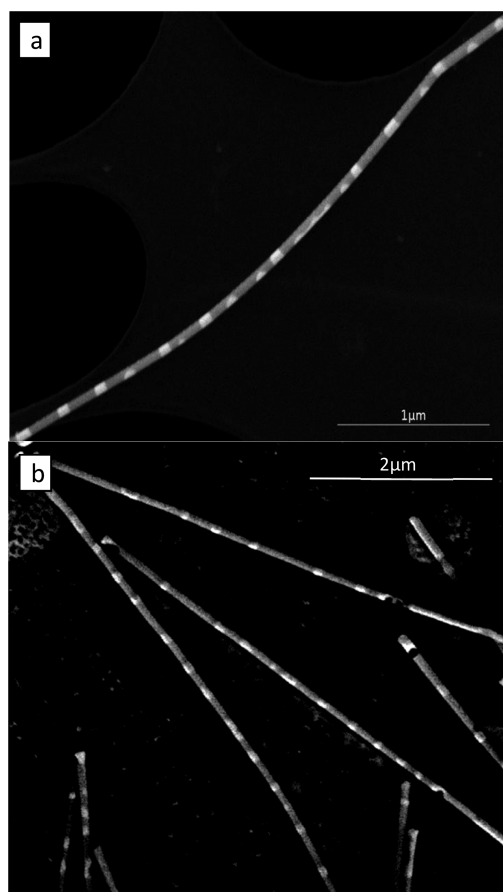


**Figure 4.** (a) SEM image of a GaAs–Au NW after FLA without preheating with an energy of 40 J/cm<sup>2</sup>. Compared to [Figure 3](#), we can see more Au segments of smaller sizes. Some superficial Au segments appear at the surface, not intercepting the entire width of the NW. (b) SEM image of a GaAs–Au NW after FLA without preheating but with a higher energy of 60 J/cm<sup>2</sup>. For better imaging, the SiO<sub>2</sub> shell was removed by buffered hydrofluoric acid.

NW. We speculate that this occurs due to a lower thermal budget, which is not sufficient to melt the entire core material.

Increasing the energy impact of the flash from 40 to 60 J/cm<sup>2</sup> yields well-contoured NWs with  $>10$  segments of axially stacked Au layers, distributed over the entire length (see [Figure 4b](#)). Obviously, the overall higher energy impact in this case enables a complete meltdown of the core NW, resulting in the fast diffusion of all Au atoms into and along the encapsulated NW.

By establishing a suitable model, we try to understand and quantify the peculiar mechanism of the phase separation in the GaAs–Au alloy, leading to rearrangement of the initial radial GaAs–Au heterostructure and its self-assembly into a sequence of axial heterostructures with perfectly sharp interfaces as a function of the temperature response of the NW. [Figure 5b](#) shows the time dependence of the NW core temperature under 20 ms FLA with 40 and 60 J/cm<sup>2</sup> power density. Details of the simulation of the temperature response of the NW during FLA are given in the [Supporting Information](#). As the GaAs–Au core is fully encapsulated in SiO<sub>2</sub>, the composition of the GaAs–Au alloy is fixed throughout the entire FLA process. Thus, the GaAs remains stoichiometric even in the liquid phase, because the desorption of As is blocked by the solid SiO<sub>2</sub> shell. This property considerably simplifies the compositional analysis

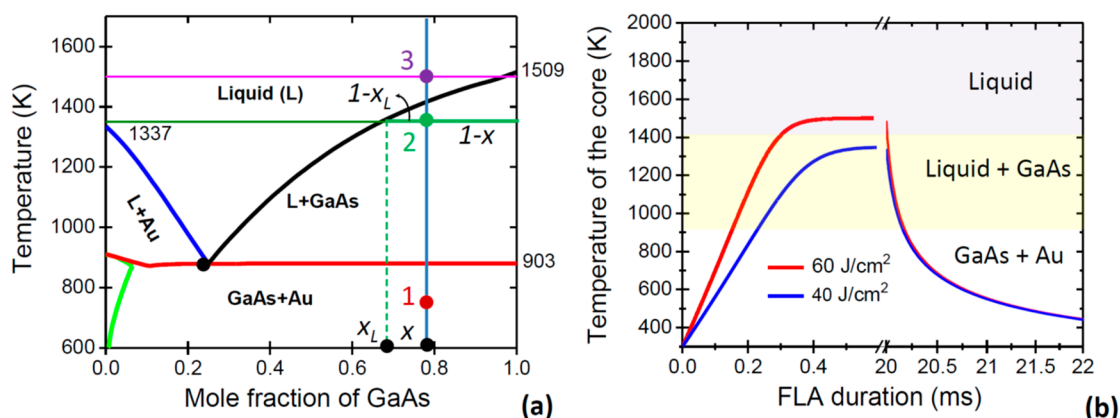


**Figure 5.** (a) Pseudobinary liquid–solid phase diagram of GaAs–Au alloy with horizontal solidus at 903 K, and the liquidus separating a mixture of GaAs–Au liquid with solid GaAs at lower temperatures from a single melt at higher temperatures. (b) Time dependence of the NW core temperature under 20 ms FLA with 40 and 60 J/cm<sup>2</sup> power density (see the Supporting Information for the parameters). The white, yellow, and pink regions in (b) mark the solid, liquid, plus solid GaAs, and pure liquid states at a fixed GaAs fraction of 0.78. It is seen that 40 J/cm<sup>2</sup> FLA leads to a maximum core temperature of 1350 K, corresponding to the incomplete melting, while increasing the FLA power to 60 J/cm<sup>2</sup> yields a temperature of 1500 K, where the alloy is completely molten. Vertical line in (a) shows heating of the core with  $x = 0.78$  from point 1, corresponding to the initial core–shell GaAs–Au NW structure, to point 2 at 1350 K under 40 J/cm<sup>2</sup> FLA and to point 3 under 60 J/cm<sup>2</sup> FLA. Horizontal green line crossing point 2 is the tie line. At 1350 K, the GaAs content in liquid GaAs–Au alloy is  $x_L$  and the fraction of liquid is  $(1 - x)/(1 - x_L)$ , whereas the fraction of remaining GaAs is  $(x - x_L)/(1 - x_L)$ . These diagrams quantitatively explain the experimental data presented in Figure 4, that is, the presence of Au clusters blocked by solid GaAs at 40 J/cm<sup>2</sup> FLA and the regular sequence of GaAs–Au axial heterostructures at 60 J/cm<sup>2</sup> FLA.

compared to the case of vapor–liquid–solid III–V NWs,<sup>28,29</sup> where highly volatile group V species easily desorb and hence their concentration in the catalyst droplet changes drastically depending on the growth conditions. Here, we can use the pseudobinary phase diagram of the GaAs–Au alloy<sup>30</sup> with stoichiometric GaAs in both liquid and solid states, as shown in Figure 5a. At least in the GaAs-rich region of the diagram, the solid state is immiscible, that is, consists of a mixture of pure GaAs and Au crystallites. Above the eutectic temperature of 903 K, the alloy consists of GaAs–Au liquid and pure GaAs crystallites with temperature-dependent fractions of liquid and the remaining solid GaAs. Above the melting temperature of GaAs of 1509 K, the GaAs–Au alloy becomes a single liquid melt, encapsulated in a SiO<sub>2</sub> shell (which remains solid below 1980 K).

It is easy to estimate the fraction of GaAs in our GaAs–Au NWs from their initial geometry. Introducing the total numbers of Au atoms  $N_{\text{Au}}$  and GaAs pairs  $N_{\text{GaAs}}$  in a core–shell NW, we have  $N_{\text{Au}}/N_{\text{GaAs}} = 2h_{\text{Au}}\Omega_{\text{GaAs}}/(R\Omega_{\text{Au}})$ , with  $h_{\text{Au}} = 2$  nm as the thickness of the Au shell layer,  $R = 36$  nm as the radius of the average GaAs core,  $\Omega_{\text{GaAs}} = 0.0452$  nm<sup>3</sup> and  $\Omega_{\text{Au}} = 0.0170$  nm<sup>3</sup> as the elementary volumes of solid GaAs and Au, respectively.<sup>31</sup> With these numbers, we obtain  $x = N_{\text{GaAs}}/(N_{\text{GaAs}} + N_{\text{Au}}) \cong 0.78$ . This determines the position of the vertical line in Figure 5a, corresponding to heating of the GaAs–Au alloy at this fixed composition. Figure 5b shows the time dependence of the NW core temperature under 20 ms FLA with 40 and 60 J/cm<sup>2</sup> power density (see the Supporting Information for the details). Moving, for example, from point 1 (corresponding to the initial core–shell GaAs–Au structure) to point 2 under FLA with 40 J/cm<sup>2</sup> (corresponding to a temperature of 1350 K according to Figure 5b) renders the system into the regime of incomplete melting. According to the lever rule,<sup>32</sup> the fraction of liquid equals  $(1 - x)/(1 - x_L)$ , whereas the fraction of solid GaAs equals  $(x - x_L)/(1 - x_L)$  with  $x_L$  as the GaAs content in liquid. The remaining solid GaAs suppresses the diffusion of Au through the volume of the

core, which explains the presence of Au clusters attached to the GaAs NW as shown in Figure 4a. By increasing the FLA power density from 40 to 60 J/cm<sup>2</sup>, we are able to cross the liquidus, which is why the alloy at 1500 K (point 3 in Figure 5a) is completely molten. This yields free diffusion of Au through the entire volume of encapsulated liquid, resulting in a more regular sequence of axial GaAs–Au heterostructures, as observed in Figure 4b.

In regard to the final stage of heterostructure formation, it occurs after stopping the FLA irradiation, where the liquid (or partially liquid) NW core rapidly cools down and becomes solid again. The width and the number of GaAs–Au heterostructures is determined by complex kinetic processes at this stage, which require a separate study. We note, however, that immiscibility of the GaAs–Au solid alloy should help to achieve atomically sharp heterointerfaces, as predicted in ref 33, for a different system (axial NW heterostructures in immiscible InAs–GaAs system). We strongly suspect that the observed segregation of In/Ga during the rapid melt growth of InGaAs<sup>22</sup> may be treated using a similar approach. Overall, our model establishes the basic mechanism for the rearrangement of encapsulated semiconductor–metal NWs (actually, of whatever initial form) into axial heterostructures under heating. It shows why the FLA power should be carefully optimized to yield the complete melting of the alloy and confirms the importance of encapsulation of the alloy within the solid SiO<sub>2</sub> shell. Melting of the core may be achieved by applying other heating techniques, and the whole procedure is expected to work equally well for a wide range of semiconductor–metal material systems.

Raman spectroscopy provides information about local strain in materials, as built-in strain leads to a characteristic shift of the phonon frequency.<sup>34</sup> By realizing spatially resolved Raman spectroscopy, variations of the strain along the NW can be measured.<sup>35,36</sup> We performed spatially resolved measurements on single GaAs–Au NWs transferred onto a Si substrate (see the Supporting Information for more details). The frequency

of the transversal optical (TO) mode along the NW length is plotted in Figure 6 as half-filled diamonds. As a reference, we

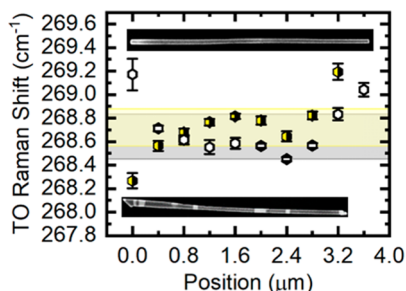


**Figure 6.** Raman shift of the TO phonon mode of GaAs along the NW length measured on a reference GaAs NW (open diamonds) and on a GaAs–Au NW (half-filled diamonds), transferred onto a Si substrate. The TO mode shifts within  $0.38\text{ cm}^{-1}$  along the reference GaAs NW (gray area) and  $0.32\text{ cm}^{-1}$  along the GaAs–Au NW (yellow area). Upper and lower insets are the SEM images of the measured GaAs and GaAs–Au NWs, respectively, taken after the Raman measurements. The SEM images are shown in the same scale as the position axis.

also measured a single pristine GaAs NW whose TO frequency along the NW length is plotted as empty diamonds. The SEM images of the measured NWs are shown in the insets of Figure 6. In both cases, the frequency of the TO mode along the NW varies within  $0.4\text{ cm}^{-1}$  with the exception of the NW ends where boundary effects and low signal-to-noise ratio affect the analysis. The full width at half-maximum (fwhm) of the TO modes varies between  $3.5$  and  $5.0\text{ cm}^{-1}$  in the case of the GaAs–Au NW and between  $3.0$  and  $4.8\text{ cm}^{-1}$  in the case of the reference GaAs NW. From these results, we can exclude any significant strain in the heterostructured NWs.

Such multiply segmented GaAs–Au NW heterostructures with abrupt interfaces should have great potential to yield a range of precisely defined electronic devices in individual NWs. Electrical contacts between metals and semiconductors are fundamentally important for devices<sup>37–39</sup> with Au–GaAs NW interfaces being of particularly interest.<sup>40</sup> Shrinking the dimensions of the contacts to the nanoscale poses significant challenges, because the properties of interfaces and even their arrangement may be very different from the conventional 2D Schottky barriers.<sup>41–46</sup> In contrast to the previous studies, our multisegmented GaAs–Au NW heterostructures resemble multiple electrical nanocontacts in series with the barrier, occurring directly and solely at the sharp heterointerface.

Performing temperature-dependent  $I/V$  measurements on six dedicated devices, exemplarily shown in the Supporting Information, we determined a remarkable low Schottky barrier height in the range of  $315 \pm 20\text{ meV}$  for these quasi 1D Au–GaAs contacts. To our knowledge, this is the lowest value of the Schottky barrier obtained for this material system. For similar NW heterostructures, namely the GaAs–Au contacts formed between the vapor–liquid–solid GaAs NW and the Au catalyst particle promoting the growth, the nanoscale contact has previously been found to alleviate the well-known Fermi-level pinning.<sup>47</sup> Thus, we explain the lowest Schottky barrier obtained here by the Fermi-level depinning, combined with the formation of an electric dipole layer at the epitaxial interface. According to ref 48, this dipole layer is formed because of the termination of GaAs NW by As atoms at the contact interface with the Au.

In conclusion, we have developed a new processing technique enabling quasi 1D GaAs–Au axial NW heterostructures. The key steps of the process include the vapor–liquid–solid growth of GaAs NWs, magnetron sputtering deposition of the Au shell, encapsulation of these core–shell NWs in  $\text{SiO}_2$  by plasma-enhanced CVD, and FLA which leads to the NW meltdown and its rearrangement into axial GaAs–Au multijunctions. This technique extends the previously reported rapid melt growth method by including Au to the semiconductor melt to obtain axial GaAs–Au heterostructures. Structural and compositional characterization has shown the excellent crystal quality and sharp GaAs–Au heterointerfaces. Revealing the physical mechanisms behind the heterostructure formation may guide future efforts to engineer nanoscale semiconductor–metal contacts with tailored electrical properties and should be applicable to a wide range of materials. In particular, the Supporting Information shows the general feasibility of the method for Si–Au, Si–NiSi, and Si–Sn material systems.

**Methods. Sample Preparation and Flash Lamp Annealing.** The GaAs NWs were grown via self-catalyzed vapor–liquid–solid growth on Si substrates by MBE. The native oxide was etched with a  $\text{HCl}/\text{H}_2\text{O}$  (1:1) solution. Subsequently, 2 nm of Au were sputtered onto the substrate and a  $\text{SiO}_2$  shell of approximately 20 nm was deposited via plasma-enhanced CVD. Finally, flash lamp annealing was carried out with different parameters. The FLA chamber was pumped to a pressure of  $10^{-5}$  mbar, and the sample was preheated for 10 min at 573 K and then exposed to a flash of 20 ms from halogen lamps with an energy impact of  $40\text{ J}/\text{cm}^2$ . This procedure was installed for Figure 1 and the multiple flash experiments. For a higher density of segments, FLA without preheating was carried out with an energy impact of  $40\text{ J}/\text{cm}^2$  (Figure 4a) and  $60\text{ J}/\text{cm}^2$  (Figure 4b).

## ■ ASSOCIATED CONTENT

### Supporting Information

The Supporting Information is available free of charge on the ACS Publications website at DOI: 10.1021/acs.nanolett.9b01076.

Further examples of metal–semiconductor heterostructures for Si–Au, Si–NiSi, and Si–Sn, demonstrating the general feasibility of the approach. Detailed description of the temperature response of the NW during FLA and a comprehensive description of the electrical measurements. Detailed Raman spectroscopy and TEM investigations, demonstrating the formation of epitaxial Au–GaAs NWs without any significant strain in the heterostructures (PDF)

## ■ AUTHOR INFORMATION

### Corresponding Author

\*E-mail: alois.lugstein@tuwien.ac.at.

### ORCID

I. Zardo: 0000-0002-8685-2305

M. Sistani: 0000-0001-5730-234X

H. Detz: 0000-0002-4167-3653

A. Lugstein: 0000-0001-5693-4775

### Author Contributions

S.B., M.B., and M.S. fabricated the samples and conducted the measurements. V.G.D. developed a model for the formation of

axial GaAs–Au heterostructures under FLA. M.S.P. performed the STEM experiments. S.L. and H.D. managed the growth of GaAs NWs. A.C. and I.Z. performed and analyzed the Raman measurements. A.L. conceived the project and contributed essentially to the experimental design. The manuscript was written through contributions of all authors. All authors have given approval to the final version of the manuscript.

### Notes

The authors declare no competing financial interest.

### ACKNOWLEDGMENTS

The authors gratefully acknowledge financial support by the Austrian Science Fund (FWF), Project Nos. P28175 and P28574 and the ESF under the project CZ.02.2.69/0.0/0.0/16\_027/0008371. The authors further thank the Center for Micro- and Nanostructures for providing the cleanroom facilities. I.Z. acknowledge financial support from the Swiss National Science Foundation research grant (Project Grant 200021\_165784). V.G.D gratefully acknowledges financial support of the Russian Foundation for Basic Research under Grants 17-52-16017, 18-02-40006, and 19-52-53031.

### REFERENCES

- Mott, N. F. *Math. Proc. Cambridge Philos. Soc.* **1938**, *34*, 568–572.
- Mott, N. F. *Proc. R. Soc. A Math. Phys. Eng. Sci.* **1939**, *171*, 27–38.
- Schottky, W. Zur Halbleitertheorie der Sperrschicht- und Spitzengleichrichter. *Eur. Phys. J. A* **1939**, *113*, 367–414.
- Schottky, W. Vereinfachte und erweiterte Theorie der Randschichtgleichrichter. *Eur. Phys. J. A* **1942**, *118*, 539–592.
- Mimura, T.; Hiyamizu, S.; Fujii, T.; et al. *Jpn. J. Appl. Phys.* **1980**, *19*, L225–L227.
- Faist, J.; Capasso, F.; Sivco, D. L.; Sirtori, C.; Hutchinson, A. L.; Cho, A. Y. *Science* **1994**, *264* (80), 553–556.
- David, L.; Bradford, C.; Tang, X.; Graham, T. C. M.; Prior, K. A.; Cavenett, B. C. *12th Int. Conf. Mol. Beam Ep.* **2002**, *251*, 261–262.
- Wofford, J. M.; Nakhaie, S.; Krause, T.; Liu, X.; Ramsteiner, M.; Hanke, M.; Riechert, H.; Lopes, J. M. *Sci. Rep.* **2017**, *7*, 1–10.
- Tourbot, G.; Bougerol, C.; Grenier, A.; Den Hertog, M.; Sam-Giao, D.; Cooper, D.; Gilet, P.; Gayral, B.; Daudin, B. *Nanotechnology* **2011**, *22* (7), 075601.
- Lari, L.; Ross, I. M.; Walther, T.; Black, K.; Cheze, C.; Geelhaar, L.; Riechert, H.; Chalker, P. R. *J. Phys.: Conf. Ser.* **2013**, *471*, 012039.
- Wolfsteller, A.; Geyer, N.; Nguyen-Duc, T. K.; Das Kanungo, P.; Zakharov, N. D.; Reiche, M.; Erfurth, W.; Blumtritt, S.; Werner, P.; Gösele, U.; et al. *Thin Solid Films* **2010**, *518*, 2555–2561.
- Wu, Y.; Xiang, J.; Yang, C.; Lu, W.; Lieber, C. M. *Nature* **2004**, *430*, 61–64.
- Joyce, H. J.; Kim, Y.; Gao, Q.; Tan, H. H.; Jagadish, C. *Proc. 2nd IEEE Int. Conf. Nano/Micro Eng. Mol. Syst. IEEE NEMS* **2007**, 567–570.
- Messing, M. E.; Wong-Leung, J.; Zanolli, Z.; Joyce, H. J.; Tan, H. H.; Gao, Q.; Wallenberg, L. R.; Johansson, J.; Jagadish, J. *Nano Lett.* **2011**, *11*, 3899–3905.
- Johansson, J.; Dick, K. A. *CrystEngComm* **2011**, *13*, 7175–7184.
- Kanungo, P. D.; Schmid, H.; Björk, M. T.; Gignac, L. M.; Breslin, C.; Bruley, J.; Bessire, C. D.; Riel, H. *Nanotechnology* **2013**, *24*, 225304.
- Borg, M.; Schmid, H.; Moselund, K. E.; Signorello, G.; Gignac, L.; Bruley, J.; Breslin, C.; Kanungo, P. D.; Werner, P.; Riel, H. *Nano Lett.* **2014**, *14*, 1914–1920.
- Borg, M.; Schmid, H.; Moselund, K. E.; Cutaia, D.; Riel, H. J. *Appl. Phys.* **2015**, *117*, 144303.
- Wagner, R. S.; Ellis, W. C. *Appl. Phys. Lett.* **1964**, *4*, 89–90.
- Liu, Y.; Deal, M. D.; Plummer, J. D.; Liu, Y.; Deal, M. D.; Plummer, J. D. *Appl. Phys. Lett.* **2004**, *84*, 2563–2565.
- Liu, Y.; Deal, M. D.; Plummer, J. D. *J. Electrochem. Soc.* **2005**, *152*, G688–G693.
- Bai, X.; Chen, C.; Mukherjee, N.; Griffin, P. B.; Plummer, J. D. *Adv. Mater. Sci. Eng.* **2016**, *2016*, 1–5.
- Liu, Z.; Wen, J.; Li, C.; Xue, C.; Cheng, B. J. *Semicond.* **2018**, *39*, 061005.
- Gallium arsenide (GaAs), Debye temperature, density, heat capacity. In *Group IV Elements, IV-IV and III-V Compounds. Part b - Electronic, Transport, Optical and Other Properties*; Madelung, O., Rössler, U., Schulz, M., Eds.; Springer: Berlin-Heidelberg, 2002; pp 1–9.
- Haas, P.; Tran, F.; Blaha, P. *Phys. Rev. B: Condens. Matter Mater. Phys.* **2009**, *79*, 1–10.
- Eränen, S. Silicon Dioxide. In *Handbook of Silicon Based MEMS Materials and Technologies*; Elsevier Inc., 2010.
- Part b: Group IV-IV and III-V Compounds. In *Impurities and Defects in Group IV Elements, IV-IV and III-V Compounds*; Madelung, O., Rössler, U., Schulz, M., Eds.; Springer, 2003.
- Glas, F. *J. Appl. Phys.* **2010**, *108*, 073506.
- Leshchenko, E. D.; Ghasemi, M.; Dubrovskii, V. G.; Johansson, J. *CrystEngComm* **2018**, *20*, 1649–1655.
- Zhang, A.; Zheng, G.; Lieber, C. M. *Nanowires: Building blocks for nanoscience and nanotechnology*; Springer, 2016.
- Dubrovskii, V. G.; Sibirev, N. V.; Cirlin, G. E.; Soshnikov, I. P.; Chen, W. H.; Larde, E.; Pareige, P.; Xu, T.; Grandidier, B.; et al. *Phys. Rev. B: Condens. Matter Mater. Phys.* **2009**, *79*, 205316.
- Smith, W. F.; Hashemi, J. *Foundations of materials science and engineering*; McGraw-Hill, 2006.
- Dubrovskii, V. G.; Koryakin, A. A.; Sibirev, N. V. *Mater. Des.* **2017**, *132*, 400–408.
- Cerdeira, F.; Buchenauer, C. J.; Pollak, F. H.; Cardona, M. *Phys. Rev.* **1972**, *5*, 580–593.
- Zardo, I.; Conesa-Boj, S.; Peiro, F.; Morante, J. R.; Arbiol, J.; Uccelli, E.; Abstreiter, G.; et al. *Phys. Rev. B: Condens. Matter Mater. Phys.* **2009**, *80*, 245324.
- Chen, J.; Conache, G.; Pistol, M.; Gray, S. M.; Borgström, M. T.; Xu, H.; Xu, H. Q.; Samuelson, L.; et al. *Nano Lett.* **2010**, *10*, 1280–1286.
- Rhoderick, E. H. *IEE Proc., Part I: Solid-State Electron Devices* **1982**, *129*, 1–14.
- Baca, A.; Ren, F.; Zolper, J.; Briggs, R.; Pearton, S. *Thin Solid Films* **1997**, *308–309*, 599–606.
- Tung, R. T. *Mater. Sci. Eng., R* **2001**, *35*, 1–138.
- Gallium Arsenide: Materials, Devices, and Circuits*; Wiley-Interscience, 1985.
- Landman, U.; Barnett, R. N.; Scherbakov, A. G.; Avouris, P. *Phys. Rev. Lett.* **2000**, *85*, 1958–1961.
- Léonard, F.; Tersoff, J. *Phys. Rev. Lett.* **2000**, *84*, 4693–4696.
- Malagù, C.; Guidi, V.; Carotta, M. C.; Martinelli, G. *Appl. Phys. Lett.* **2004**, *84*, 4158–4160.
- Léonard, F.; Talin, A. A. *Phys. Rev. Lett.* **2006**, *97*, 1–4.
- Léonard, F.; Talin, A. A. *Nat. Nanotechnol.* **2011**, *6*, 773–783.
- Coss, B. E.; Sivasubramani, P.; Brennan, B.; Majhi, P.; Wallace, R. M.; Kim, J. *J. Vac. Sci. Technol., B: Nanotechnol. Microelectron. Mater., Process., Meas., Phenom.* **2013**, *31*, 021202.
- Han, N.; Wang, F.; Yip, S.; Hou, J. J.; Xiu, F.; Shi, X.; Hui, A. T.; Hung, T.; Ho, J. C. *Appl. Phys. Lett.* **2012**, *101*, 013105.
- Suyatin, D. B.; Jain, V.; Nebořsin, V. A.; Trägårdh, J.; Messing, M. E.; Wagner, J. B.; Persson, O.; Timm, R.; Mikkelsen, A.; Maximov, I.; Samuelson, L.; Pettersson, H. *Nat. Commun.* **2014**, *5*, 1–8.